

Modelling the time-dependent rheological behaviour of heterogeneous brittle rocks

Tao Xu,^{1,2} Chun-an Tang,³ Jian Zhao,⁴ Lianchong Li³ and M. J. Heap⁵

¹Center for Rock Instability and Seismicity Research, Northeastern University, Shenyang 110819, China. E-mail: neuxutao@126.com

²State Key Laboratory of Geo-hazard Prevention and Geo-environment Protection, Chengdu University of Technology, Chengdu 610059, China

³School of Civil Engineering, Dalian University of Technology, Dalian 116024, China

⁴Laboratoire de Mécanique des Roches, Ecole Polytechnique Fédérale de Lausanne, CH-1015 Lausanne, Switzerland

⁵Laboratoire de Géophysique Expérimentale, Institut de Physique de Globe de Strasbourg (UMR 7516 CNRS, Université de Strasbourg/EOST), 5 rue René Descartes, 67084 Strasbourg cedex, France

Accepted 2012 March 14. Received 2012 January 12; in original form 2011 February 17

SUMMARY

A 2-D numerical model for brittle creep and stress relaxation is proposed for the time-dependent brittle deformation of heterogeneous brittle rock under uniaxial loading conditions. The model accounts for material heterogeneity through a stochastic local failure stress field, and local material degradation using an exponential material softening law. Importantly, the model introduces the concept of a mesoscopic renormalization to capture the co-operative interaction between microcracks in the transition from distributed to localized damage. The model also describes the temporal and spatial evolution of acoustic emissions, including their size (energy released), in the medium during the progressive damage process. The model is first validated using previously published experimental data and is then used to simulate brittle creep and stress relaxation experiments. The model accurately reproduces the classic trimodal behaviour (primary, secondary and tertiary creep) seen in laboratory brittle creep (constant stress) experiments and the decelerating stress during laboratory stress relaxation (constant strain) experiments. Brittle creep simulations also show evidence of a ‘critical level of damage’ before the onset of tertiary creep and the initial stages of localization can be seen as early as the start of the secondary creep phase, both of which have been previously observed in experiments. Stress relaxation simulations demonstrate that the total amount of stress relaxation increases when the level of constant axial strain increases, also corroborating with previously published experimental data. Our approach differs from previously adopted macroscopic approaches, based on constitutive laws, and microscopic approaches that focus on fracture propagation. The model shows that complex macroscopic time-dependent behaviour can be explained by the small-scale interaction of elements and material degradation. The fact that the simulations are able to capture a similar time-dependent response of heterogeneous brittle rocks to that seen in the laboratory implies that the model is appropriate to investigate the non-linear complicated time-dependent behaviour of heterogeneous brittle rocks.

Key words: Probability distributions; Microstructures; Creep and deformation; Acoustic properties; Mechanics, theory, and modelling.

1 INTRODUCTION

A detailed knowledge of time-dependent brittle deformation mechanisms, such as brittle creep (also known as static fatigue) and stress relaxation, is a vital prerequisite for understanding the long-term behaviour of the rocks found within the Earth’s upper crust (Karato & Li 1992; Wang *et al.* 1994). Its comprehension is therefore not only crucial for assessing geophysical hazards such as earthquake rupture (Main & Meredith 1991) and volcanic eruption (Main 1999; Kilburn 2003; Heap *et al.* 2011), but for the construction and long-term stability of engineering structures such as underground

mines and excavations (Kaiser & Morgenstern 1981; Diederichs & Kaiser 1999) and nuclear waste repositories (Nara *et al.* 2010).

Deformation during laboratory brittle creep experiments is normally explained in terms of time-dependent, subcritical crack growth (Atkinson 1984). In the Earth’s brittle upper crust, stress corrosion cracking is often considered the most prevalent subcritical crack growth mechanism (Atkinson 1982, 1984) and is powered by reactions that occur between a chemically activated geofluid (commonly water) and the strained atomic bonds at the tips of microcracks within a material (Michalske & Freiman 1982, 1983;

Freiman 1984; Hadzadeh & Law 1991). Such reactions facilitate microcrack growth (and ultimately sample failure) without the need for an increase in the applied differential stress and at lower applied differential stresses than anticipated from the short-term failure characteristics of the material. Three regimes are usually observed during brittle creep experiments (when the measured strain is plotted against time): primary creep or transient creep (decelerating strain rate), secondary creep or steady-rate creep (constant strain rate) and tertiary or accelerating creep (accelerating strain rate). The end of the tertiary creep phase is signalled by the dynamic rupture of the test sample (Scholz 1968). This kind of trimodal behaviour (note that although it is generally accepted that this behaviour is the result of subcritical crack growth, not all are exclusively interpreted in terms of stress corrosion cracking, especially carbonate rocks) has been observed in sandstone (Baud & Meredith 1997; Heap *et al.* 2009a,b; Yang & Jiang 2010), granite (Kranz 1979), basalt (Heap *et al.* 2011), oolitic iron ore (Grgic & Amitrano 2009) and limestone (Rutter 1972). In the primary creep phase, the strain rate decelerates with time via a power law. This experimental law was first observed in metals (Andrade 1910), and then for other materials, such as glass (Charles 1958; Maes *et al.* 1998), rocks (Lockner 1993b; Singh 1975) and composite materials (Nieh 1984; Tuttle & Brinson 1986; McMeeking 1993; Madgwick *et al.* 2001). The strain rate during secondary creep is considered to be essentially constant (see the ‘bath-tub’ curve, fig. 8 in Heap *et al.* 2009a) and depends strongly on the applied differential stress (see Heap *et al.* 2009a), the presence of a reactive species (Kranz *et al.* 1982; Grgic & Amitrano 2009) and the sample temperature (see Heap *et al.* 2009b). The sensitivity of the creep strain rate (the strain rate during the secondary creep phase) to the applied differential stress has been illustrated for granite (Kranz 1980; Lockner 1993b), sandstone (Baud & Meredith 1997; Ngwenya *et al.* 2001; Heap *et al.* 2009a; Yang & Jiang 2010) and basalt (Heap *et al.* 2011). In general, the experimentally derived relationship between differential stress and creep strain rate, that is, differential stress = f (creep strain rate), can be adequately fitted to either a power law or an exponential law (e.g. see Ngwenya *et al.* 2001; Heap *et al.* 2009a). The non-linearity of the process is highlighted by the values found for the exponents to these fits (for example, at an effective confining pressure of 30 MPa, the power law exponents for sandstone (Heap *et al.* 2009a) and basalt (Heap *et al.* 2011) were calculated at 45 and 32, respectively). Since brittle creep is facilitated by a chemically activated process, sample temperature has also been observed to greatly increase the creep strain rate during secondary creep (see Kranz *et al.* 1982; Heap *et al.* 2009b). Kranz *et al.* (1982) observed a decrease in the time-to-failure in brittle creep experiments on granite by up to three orders of magnitude upon increasing sample temperature from 24 to 200 °C. Similarly, Heap *et al.* (2009b) experimentally observed an increase in creep strain rate of three orders of magnitude from 20 to 75 °C in experiments on sandstones. Tertiary creep and eventual sample failure (by means of a shear fault under triaxial stress conditions) have been ascribed as the result of the sample reaching a microcrack density at which microcracks can interact and coalesce, known as the ‘critical damage threshold for tertiary creep’ (Kranz & Scholz 1977; Kemeny 1991; Baud & Meredith 1997; Miura *et al.* 2003; Heap *et al.* 2009a, 2011). A power law acceleration of strain rate has been postulated for the tertiary creep phase (Voight 1989; Main 2000). Recently, a power law model has been used to fit the tertiary creep curves for a suite of experiments on basalt at different constant applied differential stresses (Heap *et al.* 2011). Results of their maximum-likelihood model illustrate that the tertiary creep exponent shows no strain rate dependence and its value is

consistent with accelerating power law exponents observed in analogous natural systems, such as tectonic seismicity rates and seismicity and strain rates before volcanic eruptions.

Stress relaxation describes the time-dependent decay of stress within a stressed elastic body under a constant strain (i.e. the length of the sample is constant). During experimentation, the stored elastic strain energy in the test sample dissipates over a period of time through plastic deformation, allowing the value of stress supported by the sample to decay over time. Stress relaxation experiments by Rutter & Mainprice (1978) have highlighted that the strength of their sandstone samples was dramatically weakened by the presence of water at strain rates less than about 10^{-6} s^{-1} . In contrast, the strength of their dry samples showed a distinct insensitivity over a wide range of strain rates. Stress relaxation experiments on samples of tuff have shown there to be an exponential relationship between the load decay and time (Peng & Podnieks 1972). Stress relaxation tests under uniaxial compression for four rock types (conducted on a hydraulic, servo-controlled stiff testing machine) have shown that the rock stress relaxation curves exhibit two kinds of typical relaxation laws: continuity and discontinuity (Li & Xia 2000). The stress relaxation during creep convergence of a deep borehole excavated in rock salt (at depth and non-equal far-field stresses) shows that sudden failure is possible due to the slow variation of the stresses (Paraschiv-Munteanu & Cristescu 2001).

Although laboratory experiments are an essential pre-requisite for our understanding of time-dependent brittle deformation of rocks, they can be experimentally challenging due to their long (and sometimes ultra-long) duration. For example, recent data on brittle creep from Heap *et al.* (2011) demonstrated that a basalt from Mt Etna would fail after approximately 4400 min at a strain rate of $2.4 \times 10^{-9} \text{ s}^{-1}$. However, if the laboratory data are extrapolated to 10^{-10} s^{-1} , the experiment would last approximately 81 d; and at 10^{-11} s^{-1} , it would last almost two and a half years. Since such experiments can be rather unfeasible in the laboratory, modelling becomes an increasingly important tool to access the natural strain rates observed in the Earth’s brittle upper crust. A variety of approaches have been used to model the time-dependent brittle deformation of materials, including rocks. Constitutive laws, based on laboratory experiments, can provide a relation between strain, stress and strain rate (Voight 1988; Lockner 1998; Shao *et al.* 2003; Challamel *et al.* 2005). For instance, Costin (1985) developed a continuum damage model for the deformation of brittle materials based on the mechanics of microcrack nucleation and growth. The model was extended to include the effect of interaction among neighbouring microcracks during the evolution of damage. With the inclusion of interaction effects, a variety of non-linear, time-dependent behaviour such as constant stress rate loading, creep and uniaxial strain can be realistically modelled. A constitutive law consisting of a strain hardening approach with separate creep and relaxation functions has been proposed by Haupt (1991), showing that when compared with conventional steady-state creep equations, the viscous behaviour of rock salt could be described more realistically. A constitutive model for creep deformation in rock has also been derived by Shao *et al.* (2003) to describe the main time-dependent deformation features observed in cohesive frictional geomaterials (in this case, rock and concrete), such as plastic deformation, damage, volumetric dilation, pressure sensitivity, rate dependency and creep. Challamel *et al.* (2005) developed a simple time-dependent softening model to be applied to quasi-brittle materials to describe phenomena like relaxation, creep and rate-dependent loading using a unified framework. The model could be viewed as a generalization of a time-independent damage model and is based on strong

thermodynamical arguments. Models, such as those outlined above, have successfully reproduced the behaviour of different types of rocks under different loading conditions (creep, constant stress rate or strain rate). Other approaches to modelling creep involve a network of elements that interact by distributing the applied load equally among all of the intact elements, such as the concept of fibre bundles (e.g. Turcotte *et al.* 2003; Newman & Phoenix 2001). Each element represents the mesoscale, much larger than the size of one microcrack, and much smaller than the size of the system or medium. These models can only provide the temporal evolution of strain and damage during creep, and cannot model its spatial distribution, localization before failure or the size distribution of damage events. More recently, Amitrano & Helmstetter (2006) proposed a finite element model based on static fatigue laws to model the time-dependent damage and deformation of rocks under a constant stress. They used an empirical relation between time-to-failure and the applied stress to simulate the behaviour of each element. Their model produces a power law distribution of damage event sizes, aspects of localization and the trimodal behaviour seen in experimental brittle creep curves. A micromechanical model for subcritical crack growth has been proposed by Kemeny (1991), by incorporating Charles' power law relation into a 'sliding crack' model. The model reproduces the trimodal form of the creep curve, indicates that there is a critical density of microcracks at the onset of tertiary creep and allows time-to-failure predictions. At the microscopic scale, other studies have modelled the macroscopic strain using the growth of individual microcracks (Lockner & Madden 1991; Lockner 1993a). Lockner & Madden (1991) developed a numerical multiple-crack interaction model to simulate the failure process in brittle solids containing a significant population of flaws. Lockner (1993b) derived a time-dependent model for the temporal evolution of strain based on reaction rate theory and reproduced empirical laws between strain rate and stress during secondary creep. Macroscopic creep models of power law form (Charles 1958) and of exponential form (Hillig & Charles 1965; Wiederhorn & Bolz 1970) have been developed to apply the concept of stress corrosion-controlled, time-dependent cracking to large-scale geophysical problems. In practice, it can sometimes be hard to discriminate between power law and exponential rheology, due to the high stress sensitivity and the low bandwidth of stresses available (Ngwenya *et al.* 2001; Heap *et al.* 2009a). In the mean-field theory of damage mechanics, Horri & Nemat-Nasser (1985) developed a mean-field theory for the acoustic emissions (AEs) and dilatancy related to microcracking by considering a population of initially weakly interacting microcracks, with a transition to strong interactions and failure when the mean crack density reached a critical threshold. Main (2000) further developed the mean-field theory of damage mechanics and suggested a simple damage mechanics model for the apparently trimodal behaviour of the strain and event rate dependence, by invoking a phase of strain hardening involving distributed crack damage, and a phase of strain softening involving crack interaction and coalescence. The model of Main (2000) has been applied to recent experimental data sets (Heap *et al.* 2009a, 2011).

In this manuscript, we present a time-dependent material softening model to simulate the time-dependent deformation of heterogeneous brittle rocks under constant uniaxial compressional loading. We also model the accompanying AE, which is considered as a macroscopic consequence of the progressive degradation of material structure at the mesoscale. First, the time-independent model and time-dependent model are described and validated by previously published experimental data. We then present and discuss the results of our simulated brittle creep and stress relaxation experiments. Fi-

nally, the underlying mechanisms for the transition from primary to tertiary creep in heterogeneous brittle rocks are discussed using the relative roles of the renormalization, the stochastic strength field, the progressive localization and the transition from tensile to shear mechanism at different stages of damage evolution. In this work, we only present the modelling of time-dependent behaviour of heterogeneous rock in uniaxial compression. The modelling of the time-dependent behaviour of rock in triaxial loading and the extension of the model to coupled poromechanical behaviour will be the focus of future manuscripts.

2 DESCRIPTION OF THE NUMERICAL MODEL

The model is based on the theory of elastic-damage mechanics and assumes that the damage is elastic and isotropic. The model accounts for material heterogeneity through a stochastic local failure stress field, and local material degradation using an exponential material softening law (i.e. different to the approach adopted by Amitrano & Helmstetter 2006). The maximum tensile strain criterion and a modified Mohr-Coulomb criterion with a tension cut-off are adopted as two damage thresholds in the model. This approach makes it possible to simulate the transition from distributed damage by tensile microcracking to damage where microcracks can interact, coalesce and ultimately form a shear fault. The model also describes the temporal and spatial evolution of AEs, including their size (energy released), in the medium during the progressive damage process.

Our approach differs from similar models, such as Amitrano & Helmstetter (2006), by accounting for heterogeneity by allowing the material strength and Young's modulus to follow a Weibull statistical distribution. Weibull distributions are often used in the field of failure analysis due to their flexibility, and have been adopted by many researchers (Gulino & Phoenix 1991; Singh & Behrendt 1994; Tang 1997; Gupta & Bergstrom 1998; Fang & Harrison 2002; Van Mier *et al.* 2002; Xu *et al.* 2004). Amitrano & Helmstetter (2006) introduce heterogeneity by assuming that the cohesions of the elements conform to a uniform distribution. In addition, we incorporate two further statistical distributions: a uniform and normal distribution. Successful numerical simulations have previously used the Weibull distribution, normal distribution and uniform distribution to account for material strength and Young's modulus (Liang 2005). Furthermore, our model can visually replicate the temporal evolution of the shear stress fields, the associated AE and a rich assortment of other parameters, such as compressive stress, tensile stress, displacement vector, stress vector and Young's modulus during the time-dependent brittle deformation of heterogeneous rock under a constant uniaxial compressive stress.

The model therefore allows us to simulate a large range of observations from the laboratory scale (Tang 1997; Tang *et al.* 2000) to the *in-situ* macroscopic scale (Xu *et al.* 2006; Tang *et al.* 2008), and even the crustal scale (Tang *et al.* 2003). We first summarize the main features of our time-independent model, and then focus on incorporating a time dependence to the deformation.

2.1 Time-independent model

In the model, the system is analyzed at the mesoscale, and its stress-strain relationship can be described by an elastic damage constitutive law. Continuum damage mechanics can describe the effects of progressive microcracking, void nucleation and microcrack growth at high stress levels using a constitutive law, by making use of a set of state variables modifying the material behaviour at the macroscopic level. Using an isotropic continuum damage

formulation, the constitutive law for an isotropic and elastic material at instantaneous loading can be written as (Lemaitre & Chaboche 2001)

$$\varepsilon_{ij} = \frac{1 + \nu}{E} \sigma_{ij} - \frac{\nu}{E} \sigma_{kk} \delta_{ij}, \quad (1)$$

$$E = E_0(1 - D), \quad (2)$$

where ε_{ij} is the damaged elastic strain tensor, σ_{ij} is the stress tensor, E and E_0 are the Young's moduli of the damaged and the undamaged material, respectively, D is the isotropic damage variable, ν is the Poisson's ratio and δ_{ij} is the Kronecker symbol. In the case of a uniaxial state of stress ($\sigma_{11} \neq 0, \sigma_{22} = \sigma_{33} = 0$), the constitutive relation can be rewritten in terms of the longitudinal stress and strain components only:

$$\sigma_{11} = E_0(1 - D)\varepsilon_{11}. \quad (3)$$

Hence, for uniaxial loading, the constitutive law is explicitly dependent on damage index D .

The model is based on progressive isotropic elastic damage. When the stress on an element exceeds a damage threshold, its Young's modulus E is modified according to eq. (2). In the beginning, each element is considered to be elastic, defined by a specific Young's modulus and Poisson's ratio. The stress-strain curve of the element is considered linear elastic with a constant residual strength until the given damage threshold is reached. This proceeded by a phase of softening. The maximum tensile strain criterion and modified Mohr-Coulomb criterion with tension cut-off (Brady & Brown 2004; Jaeger *et al.* 2007) are selected as two damage thresholds. At any time, the tensile strain criterion is preferential since the tensile strength of rock is far lower than its compressive strength (Jaeger *et al.* 2007).

Specifically, when the mesoscopic element is under uniaxial tensile stress, the linear elastic constitutive law (with a given specific residual strength) can be illustrated as in Fig. 1. No initial damage is incorporated in this model and, in the beginning, the stress-strain curve is linear elastic and no permanent damage occurs. When the maximum tensile strain criterion is met for a given element, the element is damaged. According to the constitutive law of mesoscopic element under uniaxial tension (as shown in Fig. 1), the damage evolution of element D can be expressed as

$$D = \begin{cases} 0, & \varepsilon < \varepsilon_{t0}, \\ 1 - \frac{\sigma_{tr}}{\varepsilon E_0}, & \varepsilon_{t0} \leq \varepsilon < \varepsilon_{tu}, \\ 1, & \varepsilon \geq \varepsilon_{tu}, \end{cases} \quad (4)$$

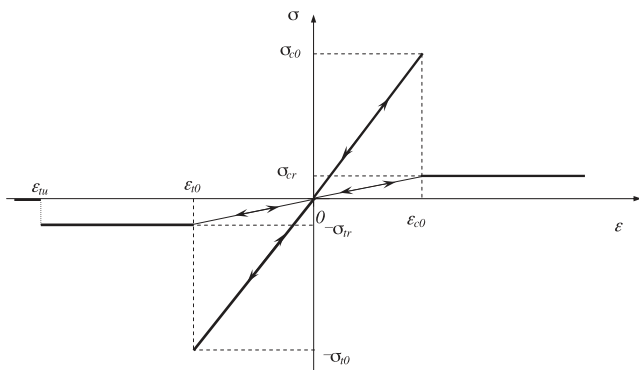


Figure 1. Elastic damage constitutive law of an element under uniaxial tensile and compressive stress.

where σ_{tr} is the residual uniaxial tensile strength and $\sigma_{tr} = \lambda\sigma_{t0}$, where λ is the residual strength coefficient and σ_{t0} is the uniaxial tensile strength at the elastic strain limit ε_{t0} . ε_{tu} is the ultimate tensile strain of the element. Eq. (4) indicates that an element would be completely damaged when the tensile strain of the element attains this ultimate tensile strain.

Since it is assumed that the damage of a mesoscopic element in a multi-axial stress field is also isotropic and elastic, the above-described constitutive law for uniaxial tensile stress can be extended to 3-D stress states. Under multi-axial stress states, an element is still damaged in a tensile mode when the equivalent strain $\bar{\varepsilon}$ (Lemaitre & Desmorat 2005) attains the aforementioned threshold strain ε_{t0} . The constitutive law for an element subjected to multi-axial stresses can be easily obtained by substituting the strain ε in eq. (4) with equivalent strain $\bar{\varepsilon}$. The equivalent strain $\bar{\varepsilon}$ is defined as follows:

$$\bar{\varepsilon} = \sqrt{\langle \varepsilon_1 \rangle^2 + \langle \varepsilon_2 \rangle^2 + \langle \varepsilon_3 \rangle^2}, \quad (5)$$

where the equivalent strain $\bar{\varepsilon} = \sqrt{\langle \varepsilon_1 \rangle^2 + \langle \varepsilon_2 \rangle^2 + \langle \varepsilon_3 \rangle^2}$, where $\varepsilon_1, \varepsilon_2$ and ε_3 are the three principal strains, $\langle \cdot \rangle$ stands for the positive part of a scalar and $\langle x \rangle = (x + |x|)/2$.

Similarly, when the element is under uniaxial compression, and damaged in shear mode according to the Mohr-Coulomb criterion, the damage variable D can be described as follows:

$$D = \begin{cases} 0, & \varepsilon > \varepsilon_{c0}, \\ 1 - \frac{\sigma_{cr}}{\varepsilon E_0}, & \varepsilon \leq \varepsilon_{c0}, \end{cases} \quad (6)$$

where σ_{cr} is the residual uniaxial compressive strength and is defined as $\sigma_{cr} = \lambda\sigma_{c0}$. In the model, it is assumed that $\sigma_{cr}/\sigma_{c0} = \sigma_{tr}/\sigma_{t0} = \lambda$ holds true when the mesoscopic element is under uniaxial compression or tension.

Shear damage occurs when an element is under multi-axial stress state and satisfies the Mohr-Coulomb criterion, and the effect of the other principal stresses in the model during damage evolution process is considered. When the Mohr-Coulomb criterion is met, the maximum compressive principal strain ε_{c0} at the peak value of the minimum principal stress is given by

$$\varepsilon_{c0} = \frac{1}{E_0} \left[f_{c0} + \frac{1 + \sin \varphi}{1 - \sin \varphi} \sigma_3 - \mu (\sigma_2 + \sigma_3) \right]. \quad (7)$$

In addition, it is assumed that the damage evolution is only related to the maximum compressive principal strain ε_1 . Therefore, the maximum compressive principal strain ε_1 of damaged element is used to substitute the uniaxial compressive strain ε in eq. (6). Thus, eq. (6) above can be extended to biaxial or triaxial stress states:

$$D = \begin{cases} 0, & \bar{\varepsilon} > \varepsilon_{c0}, \\ 1 - \frac{\sigma_{cr}}{\bar{\varepsilon} E_0}, & \bar{\varepsilon} \leq \varepsilon_{c0}. \end{cases} \quad (8)$$

From the above derivation of damage variable D (which is generally called the damage evolution law in damage mechanics) and eq. (3), the damaged Young's modulus of an element at different stress or strain levels can be calculated. The unloaded element keeps its original Young's modulus and strength prior to its strength threshold. That is to say, the element will elastically unload and no residual deformation will occur in the simulation. It must be emphasized that when $D = 1$, eq. (3) stipulates that the damaged Young's modulus will be zero, which would make the system of equations ill-posed. Therefore, a relatively small value ($1.0e-0.5$) is given for the Young's modulus under this condition.

In the absence of heterogeneity, the behaviour of the model is entirely homogenous, no damage localization occurs and the local behaviour is replicated at the macroscopic scale. Thus, it is necessary to introduce heterogeneity to obtain a collective macroscopic behaviour different from those of the elements. To reflect the material heterogeneity at a mesoscale, the mechanical parameters (e.g. strength and Young's modulus) of the mesoscopic material elements, which are assumed to be homogeneous and isotropic, are assigned randomly from the Weibull statistic distribution (Weibull 1951) as defined in the following statistic probability density function:

$$\sigma(u) = \frac{m}{u_0} \left(\frac{u}{u_0}\right)^{m-1} \exp\left[-\left(\frac{u}{u_0}\right)^m\right], \quad (9)$$

where u is the scale parameter of an individual element (such as the strength or Young's modulus) and the scale parameter u_0 is related to the average element parameter. The shape parameter m reflects the degree of material homogeneity and is defined as a homogeneity index. According to the Weibull distribution and the definition of homogeneity index, a larger m implies that more elements will have the mechanical properties similar to the mean value, resulting in a more homogeneous material. Fig. 2 shows two numerical specimens that are composed of 20 000 (200×100) square elements of the same size, produced randomly according to the Weibull distribution and using the same uniaxial compressive strength scale parameter 100 MPa. The only difference is their homogeneity indices (m). Fig. 2(a) has an m of 2, whereas Fig. 2(b) has an m of 10. In Fig. 2, the different grey scale corresponds to different values of element strength. The corresponding stochastic distribution histogram of element strength is presented in Fig. 3. It shows that the strengths of the elements are distributed in a narrower range around the mean value when m is higher. Therefore, high values of m lead to more homogeneous numerical specimens, and vice versa. Therefore, the homogeneity index is an important parameter to control the macroscopic response of a numerical specimen.

AEs are transient elastic waves generated by the rapid release of energy within a material, such as the strain energy released during microcrack propagation. Monitoring AE during deformation has become an increasingly important diagnostic tool in material science and has provided a wealth of information regarding the failure process in brittle materials. AE monitoring has shed light on the

onset of microcracking during deformation (or C' , see Wong *et al.* 1997), the evolution the spatial and temporal progression of microcracks (e.g. Knill *et al.* 1968; Ohnaka 1983; Lockner 1991; Lockner 1993a; Benson *et al.* 2007; Brantut *et al.* 2011), and can be used in failure forecasting modelling (e.g. Bell *et al.* 2011a,b). For instance, Lockner *et al.* (1991) and Lockner (1993a) analyzed catalogues of AE events recorded during compressive loading tests on rock. The events were analyzed in terms of the information they offer about the accumulated state of damage in a material. This measured damage state can be combined with a model for the weakening behaviour of cracked solids, showing that reasonable predictions of the mechanical behaviour are possible. Based on this prior knowledge, it is reasonable to assume that the number of AE events is proportional to the number of damaged elements and the strain energy released (the strain energy before and after damage) corresponds to the energy of that particular AE event (Tang 1997; Tang *et al.* 1997). In our model, we can use the output of AE to indirectly assess the damage evolution. However, it must be mentioned that aseismic damage during rock brittle creep tests could possibly occur. The sources of aseismic damage can be numerous, for example: the low surface energy of calcite, radiated energy being absorbed by neighbouring dislocation and/or intermittent dislocation flow (Weiss & Marsan 2003; Schubnel *et al.* 2006), amongst many more. Although this approximation is obviously a simplification of what occurs in reality, it has been shown that this micromechanical representation of microcracking can yield realistic patterns and can reproduce the macromechanical behaviour of heterogeneous rock.

The cumulative damage, ψ , in a given volume of rock, due to local failures, can be defined as the ratio of the volume of failed rock, V_f , to the total volume V :

$$\psi = \frac{V_f}{V} = \frac{v_e \sum_1^s n_i}{N v_e} = \frac{1}{N} \sum_1^s n_i, \quad (10)$$

where v_e is the volume of single element, s is the number of calculation steps, n_i is the number of failed elements in the i th step and N is the total number of elements in the model. For a perfectly elastic brittle material, the energy e_f released by the failure of each element can be calculated from the element peak strength:

$$e_f = \frac{\sigma_0^2}{2E} v_e, \quad (11)$$

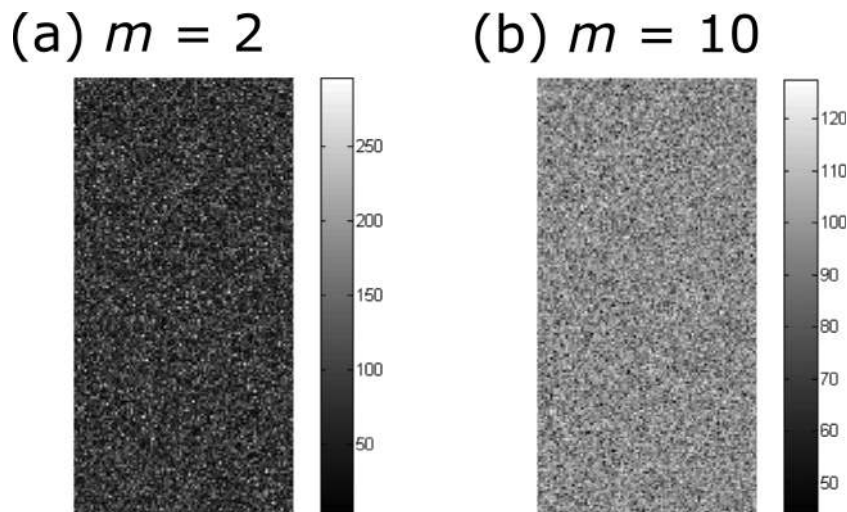


Figure 2. Numerical specimens with different strength homogeneity index m . (a) $m = 2$ and (b) $m = 10$.

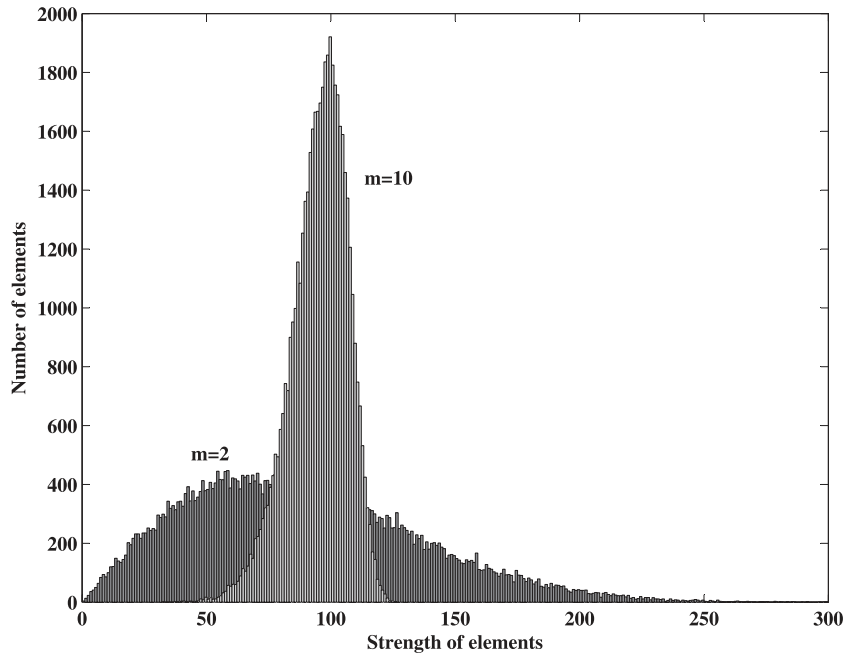


Figure 3. Histogram of the strength of an element in a numerical specimen with a different homogeneity index (m). In this example, $m = 2$ and 10 . (The numerical specimen is shown in Fig. 2, which is composed of 20 000 elements and the scale parameter u_0 is 100 MPa).

where σ_0^2 is the peak strength of the element and E is the Young’s modulus of the element. The cumulative seismic energy can then be obtained by:

$$\sum e_f = \sum \frac{\sigma_0^2}{2E} v_e = \frac{v_e}{2} \sum \frac{\sigma_0^2}{E}. \tag{12}$$

Thus, by recording the number of failed elements, the AE associated with the progressive failure of the material can be simulated in our model.

2.2 Time-dependent model

In recent studies (Pietruszczak *et al.* 2004; Shao *et al.* 2006, 2003; Amitrano & Helmstetter 2006), a general methodology has been proposed for the description of brittle creep in rock in terms of microstructural evolution. Shao *et al.* (2003) studied the time-dependent deformation of rock in terms of the evolution of microstructure leading to the progressive degradation of the Young’s modulus and the failure strength of the material. Based on these principals, they proposed a constitutive model for brittle creep deformation in rock. A time-independent creep model has also been developed based on dislocation mechanics at the continuum scale that incorporates damage to simulate the creep of metal (Esposito & Bonora 2009). Xu (1997) performed a series of brittle creep tests on weak rock in uniaxial compression and suggested that the strength and Young’s modulus of weak rock degraded with a similar law. More recently, Heap *et al.* (2010) reported the degradation of elastic moduli (Young’s modulus and Poisson’s ratio) with increasing microcrack damage in experiments on gabbro, basalt, granite and two sandstones.

As an approach to study the time-dependent deformation and failure of rock, our time-dependent model is logically formulated from the time-independent model presented above. In the model, the time-dependent behaviour of rock is considered as a macroscopic consequence of evolution of microstructure at the elementary scale. The evolution of microstructure is a time-dependent

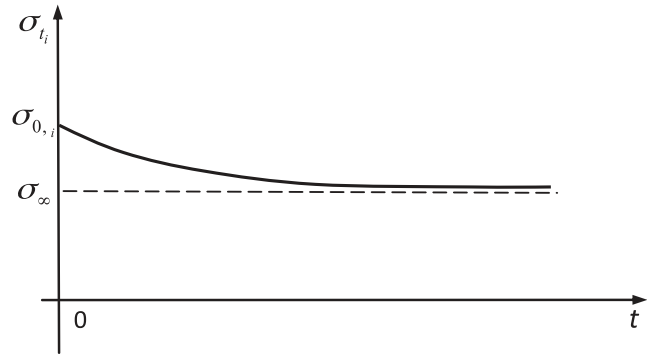


Figure 4. Schematic of the strength degradation law of an element.

progressive damage process. Based on a general understanding of time-dependent behaviour of rocks, we assume that the material degradation with time is due to the degradation of its internal material properties (such as the elastic moduli), which is attributed to microcracking within rock (Lin *et al.* 2009). We therefore introduce a material degradation law, an exponential relation between the time-dependent strength of each element and the time-to-failure of each element, to model the failure of each element when subjected to a constant stress σ_i (maximum stress on the element) smaller than its short-term strength $\sigma_{0,i}$ as shown in Fig. 4 and expressed in eq. (13):

$$\sigma_t_i = \sigma_\infty + (\sigma_{0,i} - \sigma_\infty) e^{-a_1 t_i}, \tag{13}$$

where σ_t_i is the time-dependent strength at time t_i , σ_∞ is the long-term failure strength at time t approaching infinity, $\sigma_{0,i}$ is the initial short-term failure strength of each element and a_1 is the coefficient of strength degradation of the element. An element fails either when the time t is equal to its failure time t_i , or, during an avalanche, when the stress σ_i on this element reaches the rupture criterion $\sigma_{0,i}$. The damage variable, the stress, the strength and the times-to-failure of all elements are updated after each failure event. If we let $\sigma_\infty/\sigma_{0,i} = k$, defined as the ratio of long-term failure strength to

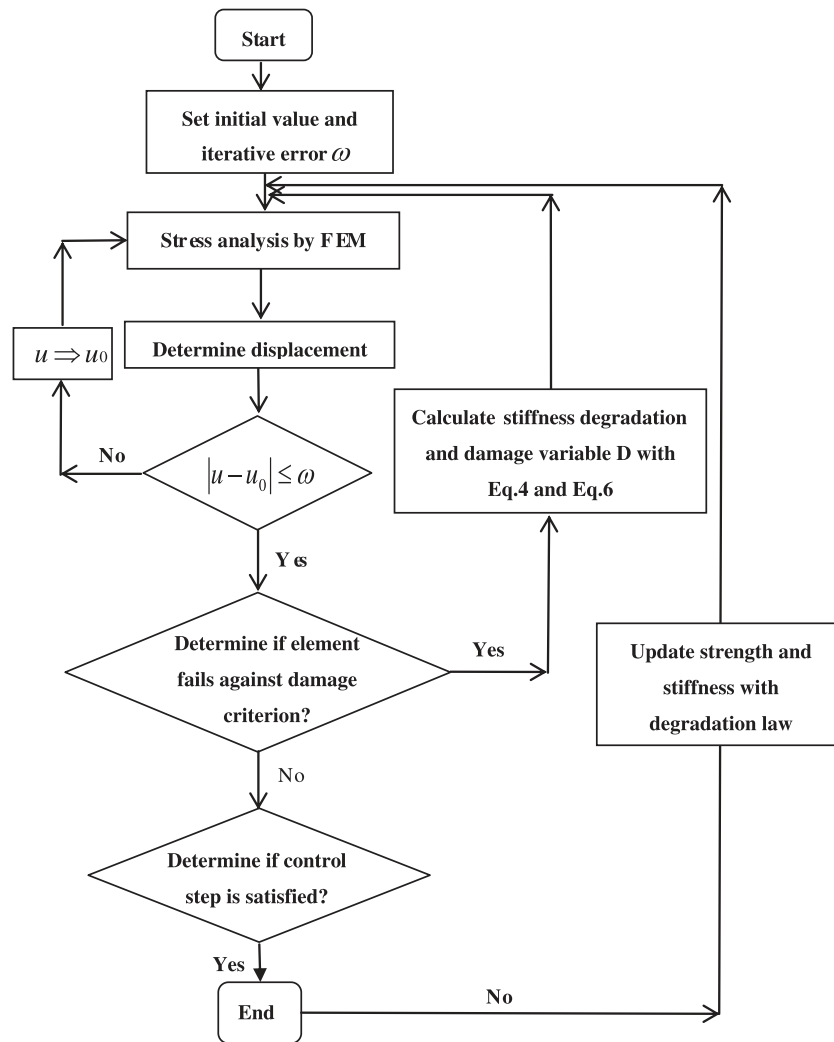


Figure 5. A flow chart for the numerical model.

the short-term failure strength, eq. (13) can be rewritten as

$$\sigma_{t_i} = \sigma_{0,i} [k + (1 - k) e^{-a t_i}]. \quad (14)$$

This is the exponential relation between the time-to-failure of each element and its normalized stress $\sigma_i/\sigma_{0,i}$. Further, the Young's modulus of each element is assumed to follow a similar degradation law as in eq. (14). The system is loaded by imposing a constant stress σ_i on its upper boundary (for brittle creep experiments). The simulation stops when the macroscopic strain reaches a threshold (after macroscopic sample failure).

To clarify the implementation of our numerical model, a flow chart of the model is shown in Fig. 5. It is important to note that eq. (14) can be easily implemented into a numerical integration algorithm using the finite element method, with nodal displacements as the principal unknowns. By introducing a time-dependent degradation of material properties into our model, the damaged behaviour with time can be obtained. In the model, the element may degrade and damage gradually with time according to the elastic damage constitutive relationship. The combined interaction of time-dependent tensile damage and compressive shear damage leads to the macroscopic failure of material. According to the general framework described above, the model can use a unified approach for the description of both short-term and long-term behaviour of heterogeneous brittle rock.

3 NUMERICAL SIMULATIONS

3.1 Geometry of the modelled samples

The geometry of the modelled sample was 100 mm × 50 mm (the same sample dimensions as in Li & Xia 2000) and was discretized into a 200 × 100 (20 000 elements) square grid (i.e. each square element had sides of 0.5 mm). The size of the modelled sample was kept constant for all of the numerical simulations throughout this paper. Steel end caps (10 mm thick and 50 mm wide) were applied to both ends of the modelled rock sample. During the simulation, the elements within the modelled rock sample are fixed in the vertical direction but can move freely in the horizontal direction (as is the case for uniaxial compressive loading).

3.2 Validation of the numerical model

The validity of our numerical model was tested via an attempt to replicate previously published experimental data from uniaxial brittle creep experiments on four different rocks (from Li & Xia 2000). The rocks used in the experimental study of Li & Xia (2000) cover a wide range of rock physico-mechanical properties (summarized in Table 1) and are therefore represent an ideal data set to test our model.

Table 1. Physico-mechanical parameters of tested rock specimens.

Rock	Uniaxial compressive strength (MPa)	Elastic modulus (GPa)	Ultimate strain (per cent)	Origin
Marble	120	70	0.23	Emei mountain,
Red sandstone	60	17	0.67	Sichuan province
Sandstone	12	3	0.52	Shenbei coal field,
Claystone	5	1.5	0.55	Liaoning province

Table 2. Physico-mechanical parameters of model specimens.

Rock	Homogeneity index	Uniaxial compressive strength (MPa)	Elastic modulus (GPa)	Poisson's ratio
Marble	2	640	95	0.25
Red sandstone	2	188	24	0.3
Sandstone	2	37.5	4.8	0.3
Claystone	2	14	2.2	0.3

The Young's modulus and the Poisson's ratio of the marble (70 GPa and 0.25, respectively) and the red sandstone (17 GPa and 0.3, respectively) were also retrieved from published literature (Wu & Zhang 2003). For the sandstone and the claystone, the Young's moduli and Poisson's ratios were estimated to be 3 GPa and 0.3 for the sandstone, and 1.5 GPa and 0.3 for the claystone. A typical brittle creep experiment involves holding a rock at a constant applied differential stress for a protracted period of time (usually until failure). For all of the experiments conducted by Li & Xia (2000), a fixed percentage (75 per cent) of the short-term peak stress was used (i.e. 90, 44, 9 and 3.75 MPa for the marble, red sandstone, sandstone and claystone, respectively). To rigorously test our model, the validation simulations were set up using the rock physico-mechanical

properties and performed at the applied differential stresses outlined above.

First, and before we can perform the numerical simulations, the mechanical parameters (such as the mean uniaxial compressive strength) for each of the model elements were obtained using a back analysis method based on both the macroscopic rock physico-mechanical properties (see Table 1) and the statistical distribution relationship between the physico-mechanical parameters of the elements at the mesoscale and the physico-mechanical properties of rock samples at the macroscale. The computed physico-mechanical parameters for elements within the modelled samples are listed in Table 2. We must note that the mesoscale element parameters listed in Table 2 represent the macroscale mechanical properties of the rock sample. The ratio of the long-term failure strength to short-term failure strength was set to 0.8 and the coefficient of degradation of each element was chosen, by trial and error, to be 0.05 s^{-1} .

The simulated creep curves (curves of strain versus time at a constant applied differential stress) are plotted in Fig. 6, together with the published experimental data of Li & Xia (2000). Fig. 6 shows that the simulated creep curves are in good agreement with the experimental creep curves. Furthermore, the simulations accurately capture the trimodal nature of a classic experimental creep curve, that is, the three creep phases (primary, secondary and tertiary), are all observed. We therefore contend that, based on these validations, our rheological model can be used to investigate the time-dependent brittle response of inhomogeneous rock under uniaxial compression loading conditions.

3.3 Modelling of basic mechanical properties

Prior to investigating brittle creep and the stress relaxation behaviour of rocks, a constant displacement rate uniaxial experiment (i.e. a conventional unconfined compressive strength experiment, or UCS experiment) was conducted numerically to obtain the macroscopic physico-mechanical properties of our studied rock. The mesoscale physico-mechanical properties of the individual elements used in

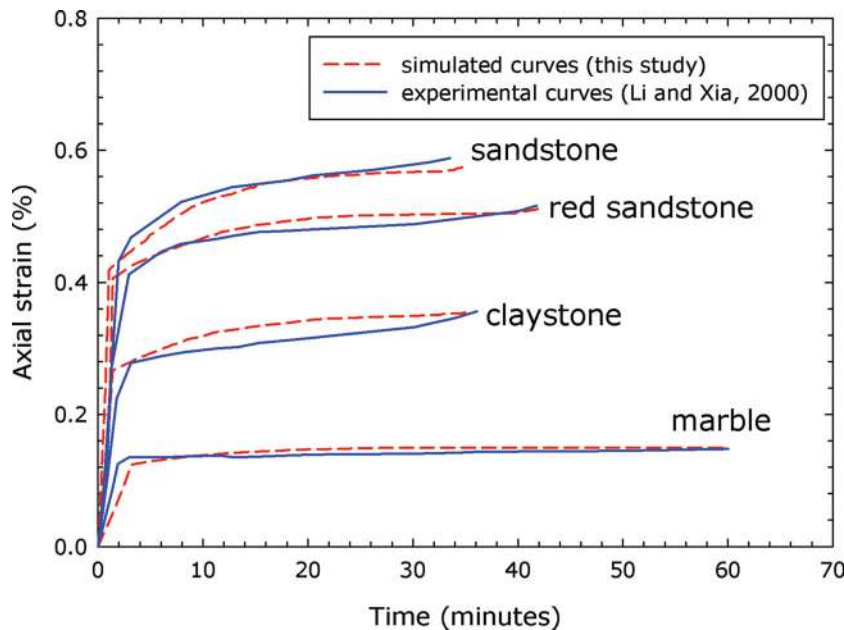
**Figure 6.** Comparison between simulated brittle creep curves (red dashed lines) and experimental brittle creep curves (blue solid lines) from Li & Xia (2000).

Table 3. Physico-mechanical parameters of numerical model.

Items	Specimen
Homogeneity index	1.5
Mean uniaxial compressive strength, MPa	200
Mean Young's modulus, MPa	60 000
Poisson ratio	0.25
Ratio of compressive to tensile strength	10
Frictional angle, °	30

the simulation are given in Table 3. The modelled sample was then uniaxially loaded under a constant displacement rate.

The simulated constant strain rate of stress–strain curve and associated AEs are shown in Fig. 7. The model accurately simulates the non-linear nature of a typical experimental constant strain rate of stress–strain curve for heterogeneous brittle rock (see Paterson & Wong 2005). The stress–strain response was first pseudo-linear (elastic, recoverable strain) prior to the onset of dilational microcracking at about 9 MPa (as evidenced by the onset of AE output), usually termed as C' (see Wong *et al.* 1997). In terms of the simulation, this represents the failure of individual elements within the grid. Furthermore, at this early stage in the deformation, the distribution of failed elements was diffused (i.e. not localized) throughout the modelled sample. After the onset of dilational microcracking, the curve deviated from pseudo-linearity as irrecoverable microcrack damage developed in the sample. Eventually, the sample failed, reaching a peak stress (maximum strength) of about 30 MPa. Sample failure was the result of the failure of clusters of elements (i.e. localized) and was accompanied by sharp burst in AE output (Fig. 7).

The modelled final shear stress fields and final AE distributions for the simulation are also shown in Fig. 7. The greyscale in the shear stress field represents the relative magnitude of the associated shear stresses, where lighter areas are indicative of higher shear stresses, and vice versa. The black areas in the shear stress field represent completely damaged elements (i.e. $D = 1$). In the AE distributions of Fig. 7, each circle symbol represents one AE event. The size of the circle represents the magnitude of the released energy and the

colour represents the type of event (white = shear crack induced by a compressive stress and red = tensile crack induced by tensile stress). A black circle represents a failed element or an AE event in a former calculating step. The detailed spatial distribution of the shear stress and the AE activity shows the location and orientation of the shear fault that ruptured the sample. In this case, failure was induced by two large conjugate shear faults (Fig. 7).

3.4 Modelling of brittle creep behaviour

The proposed model will now be used to simulate a suite of conventional brittle creep experiments under different constant applied differential stresses (i.e. we changed the ratio between the creep hold stress and the short-term failure stress). Similar to laboratory brittle creep experiments (e.g. see Heap *et al.* 2009a), the numerically simulated brittle creep experiments consisted of two stages: (1) an initial loading stage, where the sample is loaded (at the same rate) to a pre-determined level of stress and (2) a constant stress stage, where the sample is kept at a constant stress until macroscopic sample failure or until it was clear that the sample would not fail under the imposed constant stress in a reasonable time period (for further details see fig. 1 in Heap *et al.* 2011). The numerical simulations were all performed using the physico-mechanical parameters presented in Table 3 and under uniaxial compressive loading conditions. In addition to the constant displacement rate experiments described above, to simulate time-dependent behaviour, the ratio of the long-term failure strength to the short-term failure strength and the coefficient of degradation of the element were set at 0.8 and 0.05 s^{-1} , respectively. These parameters were maintained for the steel end caps so that material degradation could not occur. The constant stresses used in the simulations were 20, 21, 22, 23, 23.8, 24, 25 and 26 MPa. Since the modelled rock sample has a UCS of 30 MPa (see Fig. 7), these stresses equate to between 67 and 87 per cent of the short-term failure stress. These stress ratios are within the range where we should expect time-dependent brittle creep to occur (see Heap *et al.* 2009a). The numerically modelled creep curves (strain against time) together with the output of AE against time for all of the brittle creep experiment simulations are presented

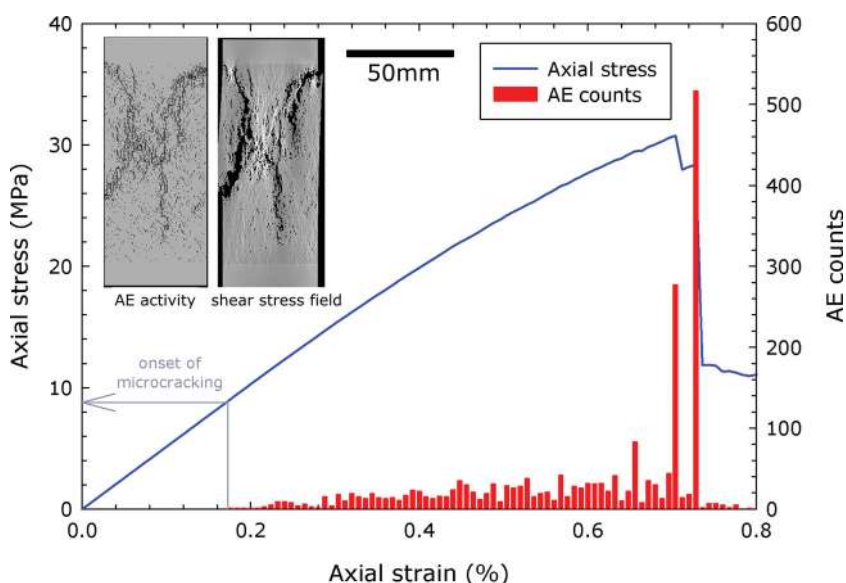


Figure 7. The stress–strain curve (solid blue line) and associated AE output (red bars) for a numerical sample deforming under a constant displacement rate in uniaxial compression. The final plots of AE activity and shear stress field are also shown on the figure (see text for details).

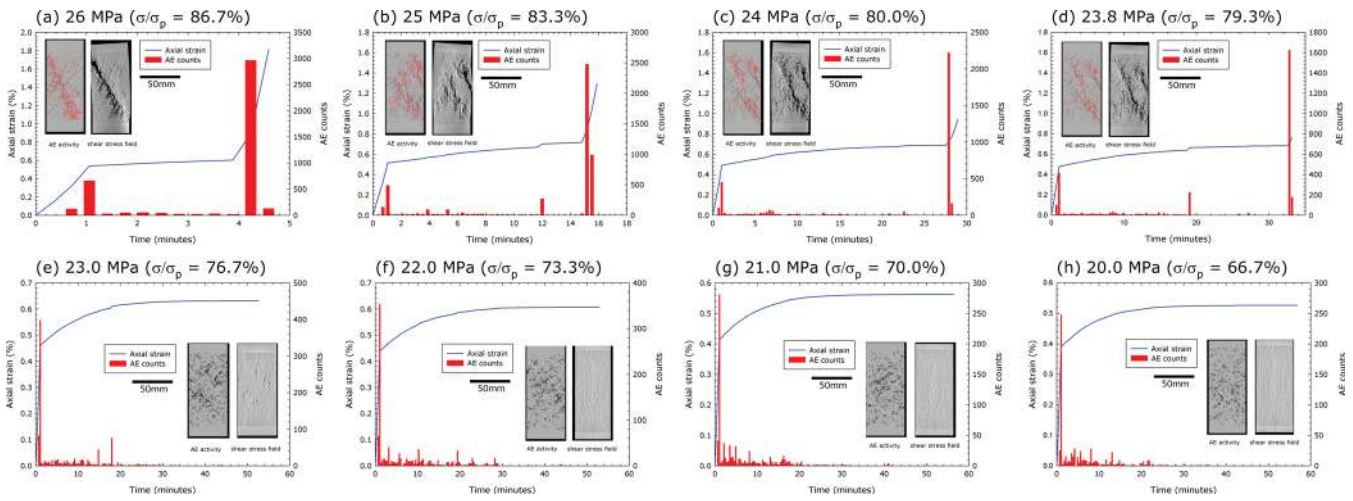


Figure 8. Creep (solid blue lines) curves and associated AE output (red bars) for constant stress simulations at constant stresses of (a) 26, (b) 25, (c) 24, (d) 23.8, (e) 23, (f) 22, (g) 21 and (h) 20 MPa. The final plots of AE activity and shear stress field are also shown on the graphs (see text for details).

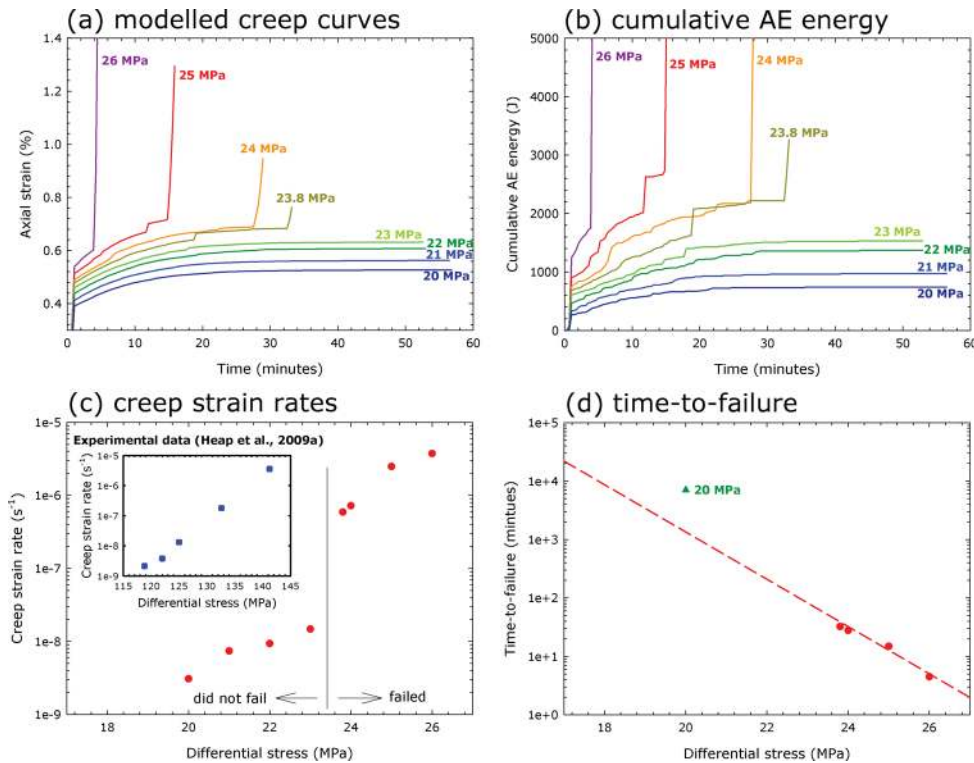


Figure 9. Synopsis plots of the simulated creep curves shown in Fig. 8, showing (a) the creep curves, (b) the cumulative AE energy, (c) the calculated creep strain rates on a log-linear plot and (d) the times-to-failure on a log-linear plot. (c) also shows some experimental data from Heap *et al.* (2009a). The green triangle in (d) is the calculated time-to-failure for the simulation at 20 MPa (see text for details).

in Fig. 8. Further, we show synopsis plots of the creep (time versus strain) curves (Fig. 9a), the cumulative output of AE energy in Joules (Fig. 9b), and the calculated creep strain rates (Fig. 9c) and times-to-failure (Fig. 9d) for all of the simulations given in Fig. 8. The results from the brittle creep simulations are also presented in Table 4.

The simulations show that for the four lowest stress levels (between 67 and 77 per cent of the short-term failure stress), sample failure was not observed in the first 55 min and the simulations were discontinued. These simulations did not result in sample failure and only the primary and secondary creep phases were observed. The

strain and output of AE energy both decelerated with time (by a power law or Andrade’s law, Andrade 1910) until both proxies for sample damage reached what appear to be near-constant values. However, in fact, the strain rates were not constant. The samples were deforming at very slow strain rates. The creep strain rates (the strain rate calculated from within steady-rate secondary creep) were 3.1×10^{-9} , 7.4×10^{-9} , 9.3×10^{-9} and $1.5 \times 10^{-8} \text{ s}^{-1}$ for the applied differential stresses of 20, 21, 22 and 23 MPa, respectively. Heap *et al.* (2009a) postulated that the lower limit for brittle creep is likely to be at the position of *C'* (the lower limit of new damage accumulation). For our simulated rock samples, the stress

Table 4. Results of the brittle creep simulations.

Applied creep stress (MPa)	Applied creep stress (per cent of the short-term peak stress)	Resultant creep strain rate (s^{-1})	Time-to-failure (min)
20	66.7	3.1×10^{-9}	–
21	70.0	7.4×10^{-9}	–
22	73.3	9.4×10^{-9}	–
23	76.7	1.5×10^{-8}	–
23.8	79.3	5.9×10^{-7}	32.4
24	80.0	7.2×10^{-7}	27.8
25	83.3	2.4×10^{-6}	14.9
26	86.7	3.7×10^{-6}	4.5

at the position of C' was about 9 MPa (Fig. 7), much lower than the minimum stress we have used in our simulations. Therefore, it is likely that although the proxies for sample damage (strain and AE energy) were progressing at very low rates, it is likely that the samples would have eventually failed if given the appropriate time. Indeed, complete conventional creep experiments have been known to last longer than 55 min (e.g. Heap *et al.* 2009a, 2011).

However, brittle sample failure was observed, and hence all three creep phases (primary, secondary and tertiary) were obtained, for the four highest levels of constant applied stress (between 79 and 87 per cent of the short-term failure stress). The strain first decelerated to a steady rate, before accelerating to failure (approximately exhibiting a power law function) after a period of time (Fig. 9a). The output of AE followed a very similar trend (Fig. 9b). In terms of the simulation, the increase in the rate of these proxies for sample damage was the result of interactions among elements and increasing damage induced by element degradation. At 86.7 per cent, the sample had a creep strain rate of $3.7 \times 10^{-6} s^{-1}$ and failed after about 4.5 min (Fig. 8a), whereas at 79.3 per cent, the creep strain rate was reduced to $5.9 \times 10^{-7} s^{-1}$ and sample failure occurred after about 32 min (Fig. 8d). It is well known that during brittle creep experiments, creep strain rate increases and time-to-failure decreases as the constant applied differential stress is increased (e.g. see Kranz 1980; Baud & Meredith 1997; Heap *et al.* 2009a, 2011); a notable feature during the deformation of heterogeneous brittle rock, since brittle fracture is a stochastic process.

The axial strain at the onset of tertiary creep for the simulations at the four highest stresses was found to be approximately equal (they each enter tertiary creep between about 0.65 and 0.70 per cent axial strain). At the onset of tertiary creep, a critical mass of failed individual elements developed, and, at that point, they began to interact (both on a local scale and through the renormalization of softening in the model) and coalesce. This resulted in strong damage localization and damage acceleration too fast for the decreasing strength reduction rate, possibly associated with an increasing proportion of shear failure events. This agrees with previously published data that postulates the existence of a ‘critical level of damage’ required before the onset of acceleration to failure, in both brittle creep experiments (Kranz & Scholz 1977; Baud & Meredith 1997; Heap *et al.* 2009a, 2011) and modelling (Kemeny 1991). These authors consider that the acceleration to sample failure is linked to the point at which microcracks can start to interact and coalesce, a feature also reproduced by our model. However, Heap *et al.* (2009a) show that the distribution of AE hypocenters during a brittle creep experiment on sandstone hints that early stages of localization could begin as early as the primary creep stage. It must be noted that the durations of the tertiary creep phase in our simulations are approximately equal, whereas experimental data (e.g. Heap *et al.* 2009a,

2011) show that the duration of the tertiary creep phase is reduced as the applied differential stress is increased. Further work will concentrate on a solution to this discrepancy and will be reported in a future manuscript.

The data from the simulated conventional brittle creep experiments can be summarized in log-linear plots of creep strain rate (Fig. 9c) and time-to-failure (Fig. 9d) versus applied differential stress. Experiments have demonstrated that the plot of creep strain rate versus differential stress forms a linear curve on a log-linear plot (see inset in Fig. 9c, experimental data for sandstone from Heap *et al.* 2009a), that can be adequately fitted with either a power law or exponential law function. However, the modelled results do not accurately replicate this behaviour and show a substantial jump in creep strain rate between 23 and 23.8 MPa. This sharp increase in creep strain rate marks the boundary between those simulations that resulted in sample failure and those that were arrested at 55 min, and therefore did not fail (marked by a line in Fig. 9c). This discrepancy cannot be due to the fact that the four experiments between 67 and 77 per cent of the short-term failure stress did not reach secondary creep, and therefore the calculated strain rates are inaccurate, as this would only serve to overestimate the strain rates. Further, if the simulations were allowed to run until sample failure, the sample at a constant stress of 20 MPa would fail after about 7000 min (calculated using the creep strain rate and the strain required to reach an axial strain of 0.65 per cent). Extrapolation from the simulations that resulted in sample failure offers a failure time between 1000 and 2000 min for 20 MPa (see Fig. 9d). Experimental data have demonstrated that this kind of extrapolation is reasonable within the range of strain rates achievable in the laboratory (Heap *et al.* 2009a, 2011). Nevertheless, the model does accurately replicate specific aspects of time-dependent brittle deformation during a conventional brittle creep experiment, such as the trimodal creep behaviour and the ‘critical level of damage’ required for the onset of tertiary creep. The solution to the problem of the sharp increase in creep strain rate between 23 and 23.8 MPa is non-trivial and future work will concentrate on resolving this discrepancy and will be reported in a subsequent manuscript.

The modelled final shear stress fields and final AE distributions for the complete range of applied differential stress levels are also shown in Fig. 8. Large discrete shear faults can be seen for the simulations at the four highest stress levels (between 79 and 87 per cent of the short-term failure stress), whereas more distributed damage can be seen for the four lowest stress levels (between 67 and 77 per cent). The detailed temporal evolution and spatial distribution of the shear stress field and the AE activity for two of the simulated brittle creep experiments are shown in Fig. 10. Fig. 10(a) shows the evolution of damage for a simulation that did not result in failure after 55 min (constant stress = 22 MPa) and Fig. 10(b) shows the evolution of damage for a simulation that resulted in failure after about 16 min (constant stress = 25 MPa). Adjacent to the shear stress field and the AE activity, images are the creep curves for both simulations, indicating the position of the time steps.

For the simulation conducted at 25 MPa (Fig. 10b), the initial state of damage (i.e. the damage incurred during the loading stage of the brittle creep simulation) was seen to be distributed throughout the sample (Fig. 10b, panel i). This was due to the wide distribution of weak elements (local minima in the strength distribution) in the modelled sample. Relatively few diffused AEs had occurred, resulting in an initial non-interacting microcrack network. Shear cracks dominated the deformation (white circles represent shear cracks and the red circles represent tensile cracks) during the initial loading of the modelled sample. As damage accumulated in the

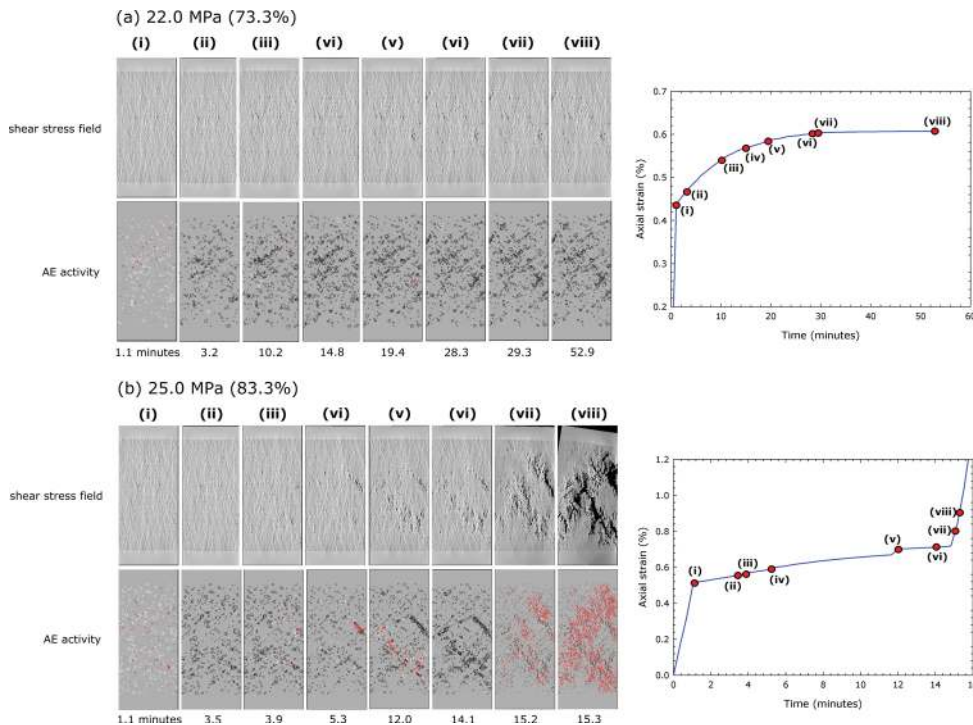


Figure 10. Snapshots of the shear stress field and the AE activity from brittle creep simulations at (a) 22 and (b) 25 MPa. The times of the snapshots are given below the panels (in minutes) and their locations on the creep curve are shown in the adjacent strain-time plots.

sample during the creep phase of the simulation, the number of distributed local minima decreased and the microcracking became increasingly clustered (Fig. 10b, panel vi), thus involving increasingly more adjacent elements, that is, microcrack interaction (both on a local scale and through the renormalization of softening in the model) and coalescence was in motion. Indeed, a localized cluster of tensile microcracking had formed in the top right of the sample after just 5.3 min. After 12 min, the focus of damage had switched to another localized zone parallel and immediately below the first cluster. As the number of failed elements increased within these two localized zones of damage, adjacent elements were exploited due to their now reduced strength (when compared to other elements far from the damaged zones). This stress concentration produced a strong damage localization that more than overcame the decreasing strength reduction rate, possibly associated with an increasing proportion of shear failure events. In other words, the clusters produced their own stress fields that dominated further microcrack growth. Eventually, the elements in and surrounding the localized zones of damage became mechanically unstable and there was the sudden collapse of sample structure, resulting in the formation of two through-going shear faults (Fig. 10b, panel viii). The ultimate failure of the sample, commensurate with a large number of small tensile microcracks, exploited both of the earlier-formed clusters of damage. The question of when damage starts to localize during a brittle creep experiment is certainly an interesting one, and has been discussed by many authors. During the initial stages of deformation, it is difficult to predict the location of the eventual shear fault. However, perhaps, the beginning stages of a localized fault plane can be observed in the 22 MPa simulation (Fig. 10a) from about 28.3 min onward, running northwest–southeast through the sample (most clearly seen in the AE activity plots). As discussed above, the same is true in the simulation conducted at 25 MPa (Fig. 10b). Using the benefit of hindsight (i.e. looking at the final panel (viii)),

we can see that damage started to localize one of the eventual fault planes after only 5.3 min (and can be seen in both the shear stress and AE activity plots). In terms of the creep curve, this corresponds to a position just after the onset of secondary steady-rate creep. These observations are in agreement with the experimental findings of Heap *et al.* (2009a) and Yanagidani *et al.* (1985). Heap *et al.* (2009a) showed that in triaxial brittle creep experiments on sandstone, AE hypocenters suggested that localization could start as early as the primary creep phase. Yanagidani *et al.* (1985) came to a similar conclusion based on uniaxial experiments on granite. However, it must be noted that there is contradictory data (Hirata *et al.* (1987) showed that clustering and localization increases as creep progresses, with the biggest changes occurring during the tertiary creep phase) and theories (e.g. the ‘critical level of damage’ theory, as explained above, suggests that the acceleration signalling the start of the tertiary creep phase is due to microcrack interaction, coalescence and localization).

In addition, the numerical simulations suggest that the evolution of strain or AE during primary and secondary creep could be used to forecast the time of macroscopic failure of material. A similar conclusion, based on creep experiments, was reached by Scholz (1972) who suggested that the only characteristic time for the evolution of the damage rate during brittle creep is the time of macroscopic failure. This is also in agreement with the experimental and analytical results of Nechad *et al.* (2005a, 2005b) for heterogeneous material. They found that the macroscopic time-to-failure was proportional to the duration of the primary creep regime.

3.5 Modelling of relaxation behaviour

Relaxation tests have been numerically conducted with different initial constant axial strain levels (160, 240, 320, 400 and 650 $\mu\epsilon$) and are presented in Fig. 11(a). The physical and mechanical parameters

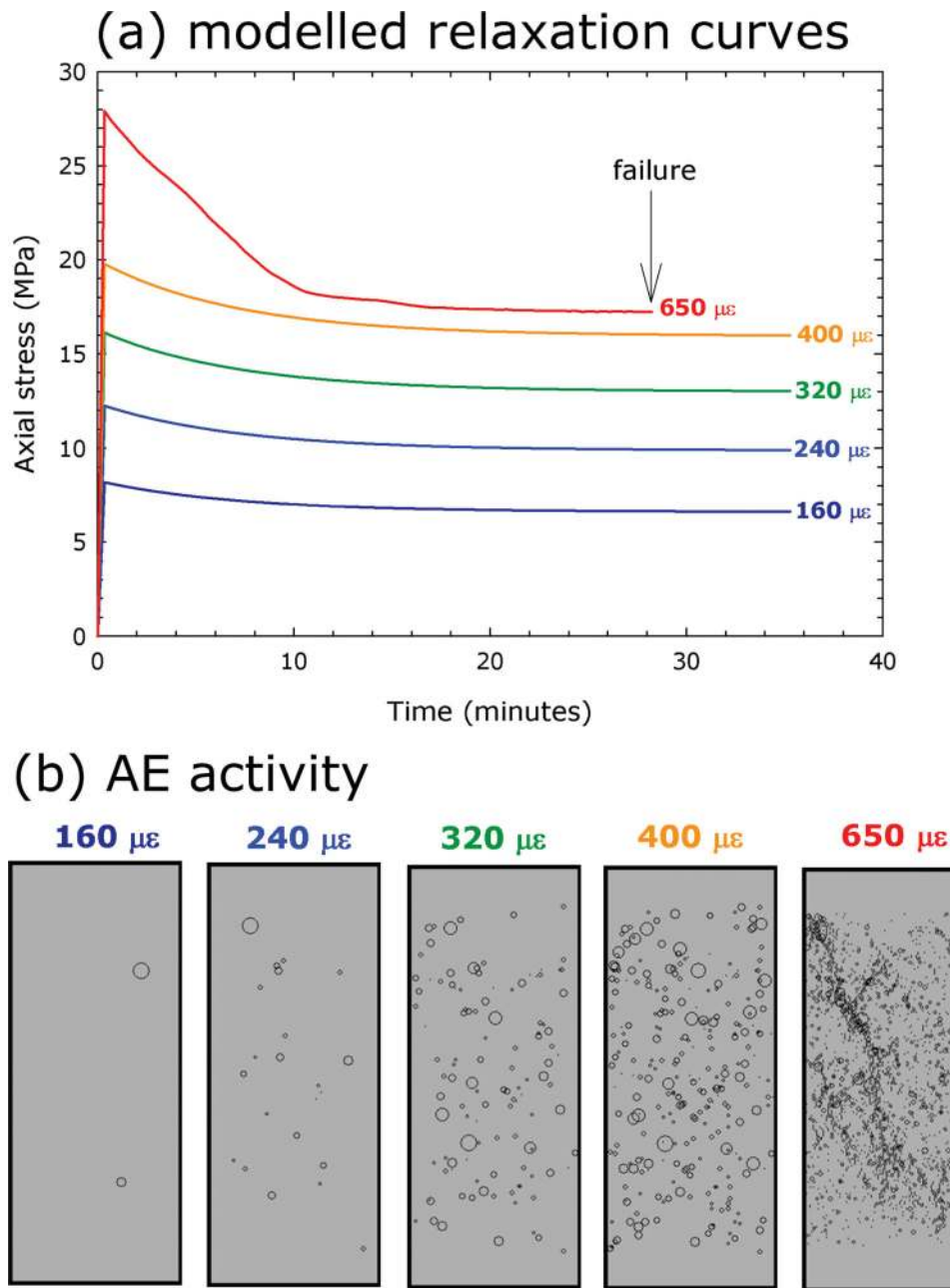


Figure 11. (a) Simulated relaxation curves for the constant strains of 160, 240, 320, 400 and 650 $\mu\epsilon$. (b) The final AE activity plots for each of the stress relaxation simulations shown in (a).

of the model specimens are the same as those used for the above brittle creep simulations (available in Table 3). The simulated samples were all loaded at the same rate. The curves of Fig. 11(a) clearly show pronounced stress relaxation over time. The total amount of stress relaxation increased when the level of constant axial strain was increased. For example, at 650 $\mu\epsilon$, the stress relaxed by about 10 MPa, whereas at 160 $\mu\epsilon$, the stress was only reduced by about 1 MPa. In all of the experiments, the rate of stress relaxation decreased during the course of the experiment; indeed, after about 30 min, with the exception of the 650 $\mu\epsilon$ curve, the curves settled down to a seemingly constant level of stress. However, the sample held at the highest constant axial strain (650 $\mu\epsilon$) failed at about 27 min (see Fig. 11b), after which the stress dropped to 0 MPa.

The final AE distributions for all five simulations are shown in Fig. 11(b). It illustrates that the number of AE events in the samples increased with increasing level of constant axial strain and, at 650 $\mu\epsilon$, the deformation was localized and a shear fault was formed. These numerical data are corroborated by the experimental studies of Li & Xia (2000).

A simulated stress relaxation curve with different strain level steps is shown in Fig. 12(a). When the first strain level of 640 $\mu\epsilon$ was applied and kept constant, the stress relaxed from point (i) (30 MPa) to point (ii) (24.8 MPa). The rate of stress relaxation decreased over time, as observed in the previous simulations (see Fig. 11a). When the second strain level of 660 $\mu\epsilon$ was applied and sustained, there was no initial increase in the axial stress, instead

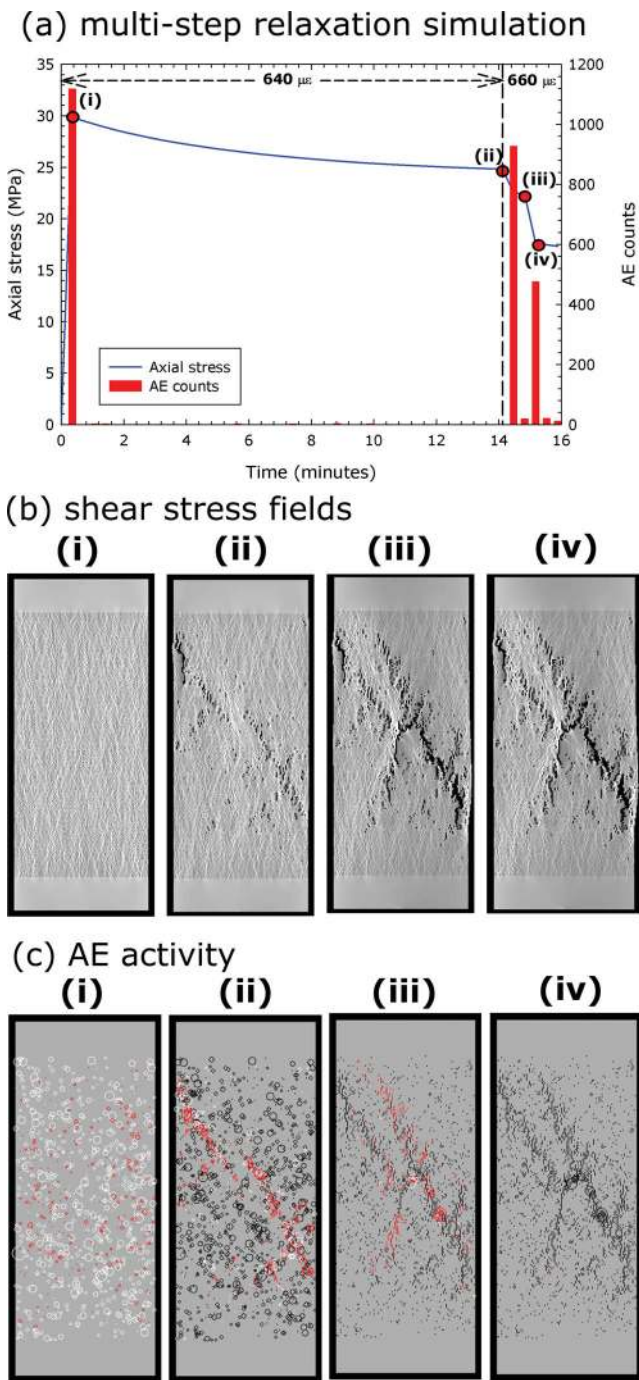


Figure 12. (a) Multistep stress relaxation simulation showing both the relaxation of the stress with time (solid blue line) and the associated AE output (red bars). (b) and (c) Snapshots of the shear stress fields and the AE activity, respectively, for the positions labelled in (a).

the stress relaxed further, and at an increased rate, from 24.8 to 22.4 MPa. The initial stage of this stress drop was commensurate with a large spike in AE activity (about 900 AEs). After about a minute had passed under a constant strain of $660 \mu\epsilon$ (point (iii)), there was another, and this time larger, stress drop accompanied by another burst of AE activity (about 500 AEs). This stress drop marked the failure of the sample. Figs 12(a) and (b) show the shear stress fields and the AE activity obtained from the experiment at points (i)–(iv) (as indicated in Fig. 11), respectively. Fig. 12(b)

shows that the AE activity associated with changing the constant level of axial strain from 640 to $660 \mu\epsilon$ was localized on the eventual failure surface. The stress drop commensurate with point (iii), which signalled the failure of the sample, extended the beginning stages of localization from point (ii) to form a through-going fault that ruptured the sample. It follows that, in nature, stress relaxation in rock should be important in regions of the crust that are highly stressed. The mechanism of stress relaxation has therefore been previously discussed in relation to earthquakes (Yang & Toksöz 1981) and volcanoes (Palano *et al.* 2009). Further, since it has been postulated that stress relaxation occurs prior to earthquake rupture (Gao & Crampin 2004; Crampin *et al.* 2008) and volcanic eruption (Bianco *et al.* 2006), an increased understanding may be useful in geophysical hazard prediction.

4 CONCLUSIONS

(1) We have presented a 2-D numerical model in an attempt to replicate the time-dependent brittle deformation of heterogeneous rock and the associated AE, under a constant uniaxial compressive stress. The model accounts for material heterogeneity through a stochastic local failure stress field, and local material degradation using an exponential material softening law. Importantly, the model introduces the concept of a mesoscopic renormalization to capture the co-operative interaction between cracks in the transition from distributed to localized damage. We have validated our model using previously published experimental data and then used it to simulate conventional brittle creep experiments and stress relaxation experiments.

(2) Our model reproduces the classic trimodal behaviour (primary, secondary and tertiary creep phases) seen in conventional laboratory brittle creep experiments. Our simulations also show evidence of the ‘critical level of damage’ before the onset of tertiary creep commonly observed in laboratory experiments, and could add to the debate as to when localization initiates during a brittle creep experiment: our modelled output shows that the initial stages of localization can be seen as early as the start of the secondary creep phase. However, when compared with experimental data, the model does not yet accurately reproduce the dependence of the applied differential stress on the creep strain rate and time-to-failure.

(3) Our model reproduces the decelerating stress relaxation during constant strain simulations. Our simulations demonstrated that the total amount of stress relaxation increased when the level of constant axial strain was increased. Our numerical data corroborate with previously published experimental data.

(4) Our approach differs from previously adopted macroscopic approaches, based on constitutive laws, and microscopic approaches that focus on fracture propagation. The model shows that the complex macroscopic time-dependent behaviour of heterogeneous brittle rocks can result from the small-scale interaction of elements and material degradation. The fact that the simulations are able to capture a similar time-dependent response of heterogeneous brittle rocks to that seen in the laboratory implies that our rheological model is appropriate to investigate the non-linear complicated time-dependent behaviour of heterogeneous brittle rocks.

(5) Our findings can be applied to the investigation of the time-dependent instability of rock masses, to the mitigation of associated rock hazards in rock engineering, and to a better understanding of geological and geophysical phenomena occurring in the Earth’s brittle upper crust.

ACKNOWLEDGMENTS

The joint supports provided by National Natural Science Foundation of China (Grant No. 41172265), the Sino-Swiss Science and Technology Cooperation Program-The Exchange Program (EG22-032009), the fund of State Key Laboratory of Geo-hazard Prevention and Geo-environment Protection, Chengdu University of Technology (SKLGP2012K008), the National Basic Research Program of China (2007CB209400) and Scientific Research Foundation for Returned Scholars, Ministry of Education of China are highly acknowledged. We would also like to thank Ian Main, one anonymous reviewer and the editor, Massimo Cocco, for comments that helped significantly improve this manuscript.

REFERENCES

- Amitrano, D. & Helmstetter, A., 2006. Brittle creep, damage, and time to failure in rocks, *J. geophys. Res.*, **111**, 1–17.
- Andrade, E.N., 1910. On the viscous flow in metals, and allied phenomena, *Proc. R. Soc. London A*, **84**, 1–12.
- Atkinson, B.K., 1982. Subcritical crack propagation in rock: theory, experimental results and applications, *J. Struct. Geol.*, **4**, 41–56.
- Atkinson, B.K., 1984. Subcritical crack growth in geological materials, *J. geophys. Res.*, **89**, 4077–4114.
- Baud, P. & Meredith, P.G., 1997. Damage accumulation during triaxial creep of darley dale sandstone from pore volumetry and acoustic emission, *Int. J. Rock Mech. Min. Sci.*, **34**, e1–e10.
- Bell, A.F., Greenough, J., Heap, M.J. & Main, I.G., 2011a. Challenges for forecasting based on accelerating rates of earthquakes at volcanoes and laboratory analogues, *Geophys. J. Int.*, **185**, 718–723.
- Bell, A.F., Naylor, M., Heap, M.J. & Main, I.G., 2011b. Forecasting volcanic eruptions and other material failure phenomena: an evaluation of the failure forecast method, *Geophys. Res. Lett.*, doi:10.1029/2011GL048155.
- Benson, P.M., Thompson, A.B., Meredith, P.G., Vinciguerra, S. & Young, R.P., 2007. Imaging slow failure in triaxially deformed Etna basalt using 3D acoustic-emission location and X-ray computed tomography, *Geophys. Res. Lett.*, doi:10.1029/2006GL028721.
- Bianco, F., Scarfi, L., Del Pezzo, E. & Patané, D., 2006. Shear wave splitting time variation by stress-induced magma uprising at Mt. Etna volcano, *Earthprints*, <http://www.earth-prints.org/handle/2122/1162>.
- Brady, B.H.G. & Brown, E.T., 2004. *Rock Mechanics for Underground Mining*, Kluwer Academic Publishers, London.
- Brantut, N., Schubnel, A. & Guéguen, Y., 2011. Damage and rupture dynamics at the brittle-ductile transition: the case of gypsum, *J. geophys. Res.*, **116**, B01404, doi:10.1029/2010JB007675.
- Challamel, N., Lanos, C. & Casandjian, C., 2005. Creep damage modelling for quasi-brittle materials, *Eur. J. Mech.*, **24**, 593–613.
- Charles, R.J., 1958. Static fatigue of glass, *J. appl. Phys.*, **29**, 1549–1560.
- Costin, L.S., 1985. Damage mechanics in the post-failure regime, *Mech. Mater.*, **4**, 149–160.
- Crampin, S., Gao, Y. & Peacock, S., 2008. Stress-forecasting (not predicting) earthquakes: a paradigm shift? *Geology*, **36**(5), 427–430.
- Diederichs, M.S. & Kaiser, P.K., 1999. Tensile strength and abutment relaxation as failure control mechanisms in underground excavations, *Int. J. Rock Mech. Min. Sci.*, **36**, 69–96.
- Esposito, L. & Bonora, N., 2009. Time-independent formulation for creep damage modeling in metals based on void and crack evolution, *Mater. Sci. Eng., A*, **510–511**, 207–213.
- Fang, Z. & Harrison, J.P., 2002. Development of a local degradation approach to the modelling of the brittle fracture in heterogeneous rocks, *Int. J. Rock Mech. Min. Sci.*, **39**, 443–457.
- Freiman, S.W., 1984. Effects of the chemical environment on slow crack growth in glasses and ceramics, *J. geophys. Res.*, **89**, 4072–4077.
- Grgic, D. & Amitrano, D., 2009. Creep of a porous rock and associated acoustic emission under different hydrous conditions, *J. geophys. Res.*, **114**, 1–19.
- Gulino, R. & Phoenix, S., 1991. Weibull strength statistics for graphite fibres measured from the break progression in a model graphite/glass/epoxy microcomposite, *J. Mater. Sci.*, **26**(11), 3107–3118.
- Gupta, V. & Bergstrom, J., 1998. Compressive failure of rocks by shear faulting, *J. geophys. Res.*, **103**(B10), 23 875–23 895.
- Hadzadeh, J. & Law, R.D., 1991. Water-weakening of sandstone and quartzite deformed at various stress and strain rates, *Int. J. Rock Mech. Min. Sci. Geomech. Abstr.*, **28**, 431–439.
- Haupt, M., 1991. A constitutive law for rock salt based on creep and relaxation tests, *Rock Mech. Rock Eng.*, **24**, 179–206.
- Heap, M.J., Baud, P., Meredith, P.G., Bell, A.F. & Main, I.G., 2009a. Time-dependent brittle creep in Darley Dale sandstone, *J. geophys. Res.*, **114**, 1–22.
- Heap, M.J., Baud, P. & Meredith, P.G., 2009b. The influence of temperature on brittle creep in sandstones, *Geophys. Res. Lett.*, doi:10.1029/2009GL039373.
- Heap, M.J., Baud, P., Meredith, P.G., Vinciguerra, S., Bell, A.F. & Main, I.G., 2011. Brittle creep in basalt and its application to time-dependent volcano deformation, *Earth planet. Sci. Lett.*, **307**, 71–82.
- Heap, M.J., Faulkner, D.R., Meredith, P.G. & Vinciguerra, S., 2010. Elastic moduli evolution and accompanying stress changes with increasing crack damage: implications for stress changes around fault zones and volcanoes during deformation, *Geophys. J. Int.*, **183**, 225–236.
- Hillig, W. & Charles, R., 1965. Surfaces, stress-dependent surface reactions, and strength, in *High Strength Materials*, pp. 682–705, ed. Zackay, V.F., Wiley, New York, NY.
- Hirata, T., Satoh, T. & Ito, K., 1987. Fractal structure of spatial distribution of microfracturing in rock, *Geophys. J. Int.*, **90**, 369–374.
- Horii, H. & Nemat-Nasser, S., 1985. Compression-induced microcrack growth in brittle solids: axial splitting and shear failure, *J. geophys. Res.*, **90**, 3105–3125.
- Jeager, J.C., Cook, N.G.W. & Zimmerman, R., 2007. *Fundamentals of Rock Mechanics*, pp. 90–94, Blackwell Publishing, Singapore.
- Kaiser, P.K. & Morgenstern, N.R., 1981. Time-dependent deformation of small tunnels—II. Typical test data, *Int. J. Rock Mech. Min. Sci.*, **18**, 141–152.
- Karato, S.-I. & Li, P., 1992. Diffusion creep in Perovskite: implications for the rheology of the lower mantle, *Science*, **255**, 1238–1240.
- Kemeny, J.M., 1991. A model for non-linear rock deformation under compression due to sub-critical crack growth, *Int. J. Rock Mech. Min. Sci. Geomech. Abstr.*, **28**, 459–467.
- Kilburn, C.R.J., 2003. Multiscale fracturing as a key to forecasting volcanic eruptions, *J. Volc. Geotherm. Res.*, **125**, 271–289.
- Knill, J.L., Franklin, J.A. & Malone, A.W., 1968. A study of acoustic emission from stressed rock, *Int. J. Rock Mech. Min. Sci. Geomech. Abstr.*, **5**, 87–88.
- Kranz, R.L., 1979. Crack growth and development during creep of Barre granite, *Int. J. Rock Mech. Min. Sci.*, **16**, 23–35.
- Kranz, R., 1980. The effect of confining pressure and stress difference on static fatigue of granite, *J. geophys. Res.*, **85**, 1854–1866.
- Kranz, R., Harris, W.J. & Carter, N.L., 1982. Static fatigue of granite at 200°C, *Geophys. Res. Lett.*, **9**, 1–4.
- Kranz, R. & Scholz, C.H., 1977. Critical dilatant volume of rocks at the onset of tertiary creep, *J. geophys. Res.*, **82**, 4893–4898.
- Lemaitre, J. & Chaboche, J.L., 2001. *Mécanique des Matériaux Solides*, 2nd edn, Dunod, Paris.
- Lemaitre, J. & Desmorat, R., 2005. *Engineering Damage Mechanics*, Springer-Verlag, Berlin.
- Li, Y.S. & Xia, C.C., 2000. Time-dependent tests on intact rocks in uniaxial compression, *Int. J. Rock Mech. Min. Sci.*, **37**, 467–475.
- Liang, Z.Z., 2005. Three-dimensional failure process analysis of rock and associated numerical test, *PhD thesis*, Northeastern University of China, Shenyang.
- Lin, Q.X., Liu, Y.M., Tham, L.G., Tang, C.A., Lee, P.K.K. & Wang, J., 2009. Time-dependent strength degradation of granite, *Int. J. Rock Mech. Min. Sci.*, **46**, 1103–1114.
- Lockner, D., 1993a. The role of acoustic-emission in the study of rock fracture, *Int. J. Rock Mech. Min. Sci.*, **30**, 883–899.

- Lockner, D., 1993b. Room temperature creep in saturated granite, *J. geophys. Res.*, **98**, 475–487.
- Lockner, D.A., 1998. A generalized law for brittle deformation of Westerly granite, *J. geophys. Res.*, **103**, 5107–5123.
- Lockner, D. & Madden, T.R., 1991. A multiple-crack model of brittle fracture. 2. Time-dependent simulations, *J. geophys. Res.*, **96**, 19 643–19 654.
- Lockner, D.A., Byerlee, J.D., Kukusenko, V., Ponomarev, A. & Sidorin, A., 1991. Quasi-static fault growth and shear fracture energy in granite, *Nature*, **350**, 39–42.
- Madgwick, A., Mori, T., Withers, P.J. & Wakashima, K., 2001. Steady-state creep of a composite, *Mech. Mater.*, **33**, 493–498.
- Maes, C., Van Moffaert, A., Frederix, H. & Strauven, H., 1998. Criticality in creep experiments on cellular glass, *Phys. Rev. B*, **57**, 4987–4990.
- Main, I.G., 1999. Applicability of time-to-failure analysis to accelerated strain before earthquakes and volcanic eruptions, *Geophys. J. Int.*, **139**, F1–F6.
- Main, I.G., 2000. A damage mechanics model for power-law creep and earthquake aftershock and foreshock sequences, *Geophys. J. Int.*, **142**, 151–161.
- Main, I.G. & Meredith, P.G., 1991. Stress corrosion constitutive laws as a possible mechanism of intermediate-term and short-term seismic quiescence, *Geophys. J. Int.*, **107**, 363–372.
- McMeeking, R.M., 1993. Power law creep of a composite material containing discontinuous rigid aligned fibers, *Int. J. Solids Struct.*, **30**, 1807–1823.
- Michalske, T.A. & Freiman, S.W., 1982. A molecular interpretation of stress corrosion in silica, *Nature*, **295**, 511–512.
- Michalske, T.A. & Freiman, S.W., 1983. A molecular mechanism for stress corrosion in vitreous silica, *J. Am. Ceram. Soc.*, **66**, 284–288.
- Miura, K., Okui, Y. & Horii, H., 2003. Micromechanics-based prediction of creep failure of hard rock for long-term safety of high-level radioactive waste disposal system, *Mech. Mater.*, **35**, 587–601.
- Nara, Y., Takada, M., Mori, D., Owada, H., Yoneda, T. & Kaneko, K., 2010. Subcritical crack growth and long-term strength in rock and cementitious material, *Int. J. Fract.*, doi:10.1007/s10704-010-9455-z.
- Nechad, H., Helmstetter, A., El Guerjouma, R. & Sornette, D., 2005a. Andrade and critical time-to-failure laws in fiber-matrix composites: experiments and model, *J. Mech. Phys. Solids*, **53**, 1099–1127.
- Nechad, H., Helmstetter, A., Guerjouma, R.E. & Sornette, D., 2005b. Creep ruptures in heterogeneous materials, *Phys. Rev. Lett.*, **94**, 045501–045504.
- Newman, W.I. & Phoenix, S.L., 2001. Time-dependent fiber bundles with local load sharing, *Phys. Rev. E*, **63**, 021 507.
- Ngwenya, B., Main, I., Elphick, S., Crawford, B. & Smart, B., 2001. A constitutive law for low-temperature creep of water-saturated sandstones, *J. geophys. Res.*, **106**, 21 811–21 826.
- Nieh, T., 1984. Creep rupture of a silicon carbide reinforced aluminum composite, *Metall. Mater. Trans. A*, **15**, 139–146.
- Ohnaka, M., 1983. Acoustic emission during creep of brittle rock, *Int. J. Rock Mech. Min. Sci. Geomech. Abstr.*, **20**, 121–134.
- Palano, M., Gresta, S. & Puglisi, G., 2009. Time-dependent deformation of the eastern flank of Mt. Etna: after-slip or viscoelastic relaxation? *Tectonophysics*, **473**, 300–311.
- Paraschiv-Munteanu, I. & Cristescu, N.D., 2001. Stress relaxation during creep of rocks around deep boreholes, *Int. J. Eng. Sci.*, **39**, 737–754.
- Paterson, M.S. & Wong, T.-F., 2005. *Experimental Rock Deformation—The Brittle Field*, Springer, New York, NY.
- Peng, S. & Podnieks, E.R., 1972. Relaxation and the behavior of failed rock, *Int. J. Rock Mech. Min. Sci. Geomech. Abstr.*, **9**, 699–700.
- Pietruszczak, S., Lydzba, D. & Shao, J.F., 2004. Description of creep in inherently anisotropic frictional materials, *J. Eng. Mech. ASCE*, **130**, 681–690.
- Rutter, E.H., 1972. On the creep testing of rocks at constant stress and constant force, *Int. J. Rock Mech. Min. Sci. Geomech. Abstr.*, **9**, 191–195.
- Rutter, E.H. & Mainprice, D.H., 1978. The effect of water on stress relaxation of faulted and unfaulted sandstone, *Pageoph*, **116**, 634–654.
- Scholz, C.H., 1968. Mechanism of creep in brittle rock, *J. geophys. Res.*, **73**, 3295–3302.
- Scholz, C.H., 1972. Static fatigue of quartz, *J. geophys. Res.*, **77**, 2104–2114.
- Schubnel, A., Walker, E., Thompson, B.D., Fortin, J., Guéguen, Y. & Young, R.P., 2006. Transient creep, aseismic damage and slow failure in Carrara marble deformed across the brittle-ductile transition, *Geophys. Res. Lett.*, **33**, L17301, doi:10.1029/2006GL026619.
- Shao, J.F., Chau, K.T. & Feng, X.T., 2006. Modeling of anisotropic damage and creep deformation in brittle rocks, *Int. J. Rock Mech. Min. Sci.*, **43**, 582–592.
- Shao, J.F., Zhu, Q.Z. & Su, K., 2003. Modeling of creep in rock materials in terms of material degradation, *Comput. Geotech.*, **30**, 549–555.
- Singh, D.P., 1975. A study of creep of rocks, *Int. J. Rock Mech. Min. Sci.*, **12**, 271–276.
- Singh, M. & Behrendt, D., 1994. Microstructure and mechanical properties of reaction-formed silicon carbide (RFSC) ceramics, *Mater. Sci. Eng., A*, **187**(2), 183–187.
- Tang, C.A., 1997. Numerical simulation of progressive rock failure and associated seismicity, *Int. J. Rock Mech. Min. Sci.*, **34**, 249–261.
- Tang, C.A., Chen, Z.H., Xu, X.H. & Li, C., 1997. A theoretical model for Kaiser effect in rock, *Pure appl. Geophys.*, **150**, 203–215.
- Tang, C.A., Huang, M.L. & Zhao, X.D., 2003. Weak zone related seismic cycles in progressive failure leading to collapse in brittle crust, *Pure appl. Geophys.*, **160**, 2319–2328.
- Tang, C.A., Tham, L.G., Lee, P.K.K., Tsui, Y. & Liu, H., 2000. Numerical studies of the influence of microstructure on rock failure in uniaxial compression—part II: constraint, slenderness and size effect, *Int. J. Rock Mech. Min. Sci.*, **37**, 571–583.
- Tang, C.A. et al., 2008. Fracture spacing in layered materials: a new explanation based on two-dimensional failure process modeling, *Am. J. Sci.*, **308**, 49–72.
- Turcotte, D.L., Newman, W.I. & Shcherbakov, R., 2003. Micro and macroscopic models of rock fracture, *Geophys. J. Int.*, **152**, 718–728.
- Tuttle, M.E. & Brinson, H.F., 1986. Prediction of the long-term creep compliance of general composite laminates, *Exp. Mech.*, **26**, 89–102.
- Van Mier, J.G.M., Van Vliet, M.R.A. & Wang, T.K., 2002. Fracture mechanisms in particle composites, statistical aspects in lattice type analysis, *Mech. Mater.*, **34**, 705–724.
- Voight, B., 1988. A method for prediction of volcanic eruption, *Nature*, **332**, 125–130.
- Voight, B., 1989. A relation to describe rate-dependent material failure, *Science*, **243**, 200–203.
- Wang, J.N., Hobbs, B.E., Ord, A., Shimamoto, T. & Toriumi, M., 1994. Newtonian dislocation creep in quartzites: implications for the rheology of the lower crust, *Science*, **265**, 1204–1206.
- Weibull, W., 1951. A statistical distribution function of wide applicability, *J. appl. Mech.*, **18**, 293–297.
- Weiss, J. & Marsan, D., 2003. Three-dimensional mapping of dislocation avalanches: clustering and space/time coupling, *Science*, **299**, 89–92.
- Wiederhorn, S. & Bolz, L., 1970. Stress corrosion and static fatigue of glass, *J. Am. Ceram. Soc.*, **53**, 543–548.
- Wong, T.-F., David, C. & Zhu, W., 1997. The transition from brittle faulting to cataclastic flow in porous sandstones: mechanical deformation, *J. geophys. Res.*, **102**, 3009–3025.
- Wu, G. & Zhang, L., 2003. A damage mechanical constitutive model of unloading failure for brittle-elastic rock mass, in *Environmental Rock Engineering*, pp. 279–283, eds. Saito, T. & Murata, S., Swets & Zeitlinger B.V., Lisse.
- Xu, H., 1997. Time-dependent behaviours of strength and elasticity modulus of weak rock, *Chin. J. Rock Mech. Eng.*, **16**, 246–251.
- Xu, X.H., Ma, S.P., Xia, M.F., Ke, F.J. & Bai, Y.L., 2004. Damage evaluation and damage localization of rock, *Theor. Appl. Fract. Mech.*, **42**, 131–138.
- Xu, T., Tang, C.A., Yang, T.H., Zhu, W.C. & Liu, J., 2006. Numerical investigation of coal and gas outbursts in underground collieries, *Int. J. Rock Mech. Min. Sci.*, **43**, 905–919.
- Yanagidani, T., Ehara, S., Nishizawa, O., Kusunose, K. & Terada, M., 1985. Localization of dilatancy in Ohshima granite under constant uniaxial stress, *J. geophys. Res.*, **94**, 6840–6858.
- Yang, S. & Jiang, Y., 2010. Triaxial mechanical creep behavior of sandstone, *Min. Sci. Technol.*, **20**, 339–349.
- Yang, M. & Toksöz, M.N., 1981. Time-dependent deformation and stress relaxation after strike slip earthquakes, *J. geophys. Res.*, **86**(B4), 2889–2901.